



Structural characterization and ZFC/FC magnetization study of $\text{La}_{0.6}\text{Ca}_{0.4-x}\text{Sr}_x\text{MnO}_3$ nanoparticle compounds

M. Jeddi¹ · H. Gharsallah^{1,2} · M. Bekri³ · E. Dhahri¹ · E. K. Hlil⁴

Received: 25 August 2019 / Accepted: 26 November 2019 / Published online: 5 December 2019
© Springer-Verlag GmbH Germany, part of Springer Nature 2019

Abstract

Structural and magnetic properties of $\text{La}_{0.6}\text{Ca}_{0.4-x}\text{Sr}_x\text{MnO}_3$ manganites have been investigated for $x=0.0, 0.1$ and 0.4 . The Rietveld analysis of X-ray diffraction data indicates that, with increasing Sr content, a structural phase transition from rhombohedral to orthorhombic is occurred. Structural parameters are calculated and found to be dependent upon the composition. The nanometric size of our samples estimated using Debye–Scherrer equation is confirmed by SEM images. Magnetic measurements according to the zero-field cooled and field cooled procedures are performed. The observed irreversibility between the two modes is assigned to the presence of magnetic anisotropy which has been explained as arising from the surface effects. The blocking temperature (T_B) is estimated and found to increase as the particle size increases. Above T_B , the materials show a superparamagnetic (SPM) behavior where the coercivity and remanence magnetizations are almost zero that favors their application in the biomedical field. Studying the thermal variation of dc susceptibility confirms the SPM nature of the studied compounds. The good fit of the magnetization vs. magnetic field curves with Langevin function supports our findings. From this simulation, the saturation magnetization is calculated and found to increase as particle size increases which is explained in terms of Core–shell model. With the reduction of particle size to the nanometric scale, single domain structure and SPM regime structure are detected.

1 Introduction

The physics of nanoscale magnetic materials have attracted a great deal of interest in recent years due to their wide ranging applications such as magnetic sensors, magnetic recording media, permanent magnets, ferrofluids, and in biomedicine [1–3]. When the size of magnetic particle decreases to a few nanometers, the energy necessary to divide itself into magnetic domains is greater than the energy needed to remain as a single magnetic domain [4], resulting in a transition from the usual multidomain structure of the bulk

to a monodomain structure. For a particle size smaller than the single domain size, the spins are progressively affected by the thermal fluctuations, and fundamentally, a ferromagnetic material becomes superparamagnetic. In the superparamagnetic regime, each particle behaves like a paramagnetic atom, but with a superspin [5]. When a superparamagnetic regime is achieved, the magnetization direction of the nanoparticle rapidly fluctuates between the opposite directions of the magnetization easy axis. The typical time between two flips is called the Neel relaxation time [6]. The temperature, at which the magnetic anisotropy energy of a nanoparticle is overcome by thermal activation and the whole system becomes superparamagnetic, is known as the blocking temperature (T_B) [7, 8]. Blocking temperature is one of the superparamagnetic properties that depends on the size of nanoparticles [9]. Above the blocking temperature, the material shows no hysteresis which is the criterion of superparamagnetism phenomenon.

Superparamagnetic materials have a wide range of applications, especially their biomedical applications are noteworthy, such as use in treatments (targeted drug delivery) [10, 11], in magnetic hyperthermia [12–14], and in imaging (contrast for magnetic resonance imaging (MRI))

✉ M. Jeddi
marwajeddi@gmail.com

¹ Laboratoire de Physique Appliquée, Faculté des Sciences, Université de Sfax, B. P. 1171, 3000 Sfax, Tunisie

² Institut Préparatoire aux Études d'Ingénieur de Sfax, Université de Sfax, B. P. 1172, 3018 Sfax, Tunisie

³ Physics Department, Rabigh College of Science and Art, King Abdulaziz University, P.O. Box 344, Rabigh 21911, Saudi Arabia

⁴ Institut Néel, CNRS Université J. Fourier, B. P. 166, 38042 Grenoble, France

[15, 16]. Hundreds of magnetic materials with considerable biomedical applications were found, and still today, dozens of new materials are described every year.

Many researchers have focused on complex metal oxides based on Fe ions with perovskite, spinel, and magnetoplumbite structure [17, 18]. These materials have attractive interest for studying due to their physical properties which are important for many applications that are required, such as use in hyperthermia. One of the most attractive systems for research are the hexaferrite materials. Due to their high functional properties, Trukhanov et al. [19, 20] have deeply reported the structural and magnetic properties of ferrites with hexagonal crystal structure substituted by different cations which are prepared by the conventional solid reaction method. Also, Almessiere et al. [21] have evaluated the magnetic properties of nanohexaferrites synthesized by the citrate sol–gel autocombustion approach. Excellent chemical stability and corrosion resistance of hexaferrites make them environmentally safe and fit for use practically without restriction in time. From a practical standpoint, hexagonal ferrites have great potential as materials for high-frequency electromagnetic applications.

Nowadays, perovskite manganese oxides with formula $R_{1-x}A_xMnO_3$ (where R is a trivalent rare earth ion and A is a divalent alkali earth ion) have been the focus of intense research due to their impressive physical properties [22–30]. Numerous convincing arguments confirm that perovskite-based manganite compounds will perform a crucial role in the upcoming technologies of the near future. Recently, lanthanum strontium manganites with a typical composition of $La_{1-x}Sr_xMnO_3$ (LSMO) are considered as a valuable research subject in this context [31–36]. The increasing attention on LSMO magnetic nanoparticles is attributed to their wide range of T_c from 283 to 380 K, biocompatibility and superparamagnetic nature [37, 38]. Some researchers have discussed about the prospects of $La_{0.67}Sr_{0.33-x}K_xMnO_3$ (LSKMO) nanoparticle compounds prepared using sol–gel method as suitable candidates for hyperthermia treatments [39]. Horiki et al. [40] have reported that $La_{0.666}Sr_{0.373}Mn_{0.943}Cu_{0.018}O_3$ compounds are promising heating mediators for inducing magnetic hyperthermia. Other studies have argued about the properties of $La_{1-x}Ag_xMnO_{3-\delta}$ nanoparticles [41, 42], as effective heating candidates for magnetic hyperthermia purposes. Obviously, several nanosized manganites have been fully characterized with deep study of the most intimate details of the structural, magnetic and other characteristic properties, but to the best of our knowledge, the superparamagnetic behavior of $La_{0.6}Ca_{0.4-x}Sr_xMnO_3$ (LCSMO) nanoparticle compounds has not been studied yet.

In this study, a systematic investigation of the structural and magnetic characteristics of $La_{0.6}Ca_{0.4}MnO_3$ ($x=0.0$),

$La_{0.6}Ca_{0.3}Sr_{0.1}MnO_3$ ($x=0.1$) and $La_{0.6}Sr_{0.4}MnO_3$ ($x=0.4$) is presented.

2 Experiment

The $La_{0.6}Ca_{0.4-x}Sr_xMnO_3$ compounds were synthesized using the citric–gel method [43]. The starting precursors: $La(NO_3)_3 \cdot 6H_2O$, $Ca(NO_3)_2 \cdot 4H_2O$, $Mn(NO_3)_2 \cdot 6H_2O$, and $Sr(NO_3)_2$ were dissolved in distilled water. To obtain a transparent stable solution, the citric acid and the ethylene glycol were added. After pre-annealing the mixture at 80 °C to eliminate excess water, the solution was annealed at 120 °C. The obtained powder was calcined at 700 °C for 12 h. Finally, the powder was pressed into pellets and sintered at 900 °C for 18 h.

The structure and phase purity of the prepared specimens were verified using the powder X-ray diffraction technique with $CuK\alpha$ radiation ($\lambda = 1.5406 \text{ \AA}$), at room temperature, by a step scanning of 0.015° in the range of $20^\circ \leq 2\theta \leq 80^\circ$. Grain size determination was carried out using a scanning electron microscope (SEM). The elemental composition of compounds was checked by the energy-dispersive X-ray analysis (EDAX). Magnetic measurements were performed by BS1 and BS2 magnetometers developed in Louis Neel Laboratory of Grenoble. The measurements of magnetization vs. temperature $M(T)$, in the zero-field cooled/field cooled (ZFC/FC) modes, were obtained under an applied magnetic field of 0.05 T with a temperature ranging from 5 to 450 K. In this kind of experiment, the samples were initially cooled to 5 K, in the absence of a magnetic field (ZFC). At 5 K, a magnetic field of 0.05 T was applied and the sample was then heated to the desired temperature. The sample is then cooled again to the lowest temperature with the constant field still applied (FC). $M_{ZFC}(T)$ and $M_{FC}(T)$ were measured during heating at intervals of no more than 5 K. In our measurements, the typical time window $\Delta t \approx 100$ s. The isothermal magnetization curves $M(\mu_0H)$ were measured at a temperature of 5 K under an applied magnetic field varying from 0 to 10 T. The hysteresis cycles were performed at a temperature slightly below the Curie temperature and at magnetic fields between -10 and 10 T.

3 Results and discussion

3.1 Structural and microstructural properties

The X-ray diffraction (XRD) patterns of our synthesized samples are depicted in Fig. 1a. It is worthy highlighting that, with increasing Sr concentration, the diffraction peaks' positions shift towards lower angle side (inset Fig. 1a). Rietveld refinement of the XRD patterns using

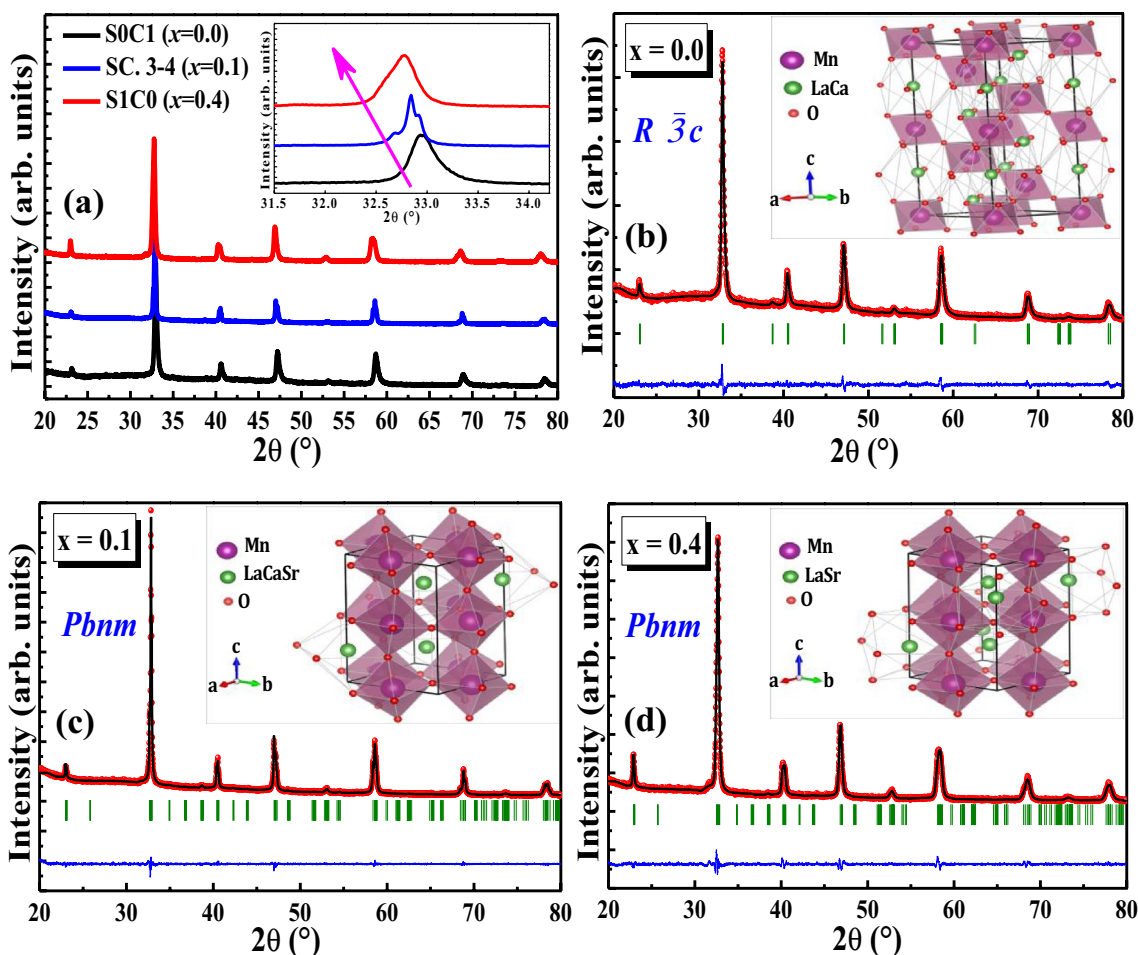


Fig. 1 a Powder XRD patterns of $\text{La}_{0.6}\text{Ca}_{0.4-x}\text{Sr}_x\text{MnO}_3$ ($x=0.0, 0.1$ and 0.4) compounds. The inset shows a zoom of the most intense peaks. Rietveld refinement of **b** $x=0.0$, **c** $x=0.1$ and **d** $x=0.4$. The inset exhibits the crystal structure

Fullprof program [44] are presented in Fig. 1b–d. The fitting between the observed and the calculated diffraction profiles shows an excellent agreement, taking into consideration the low values of the tolerance factor χ^2 (Table 1). All samples are single phase without any trace of impurity confirming the high purity of the product materials. As shown in Fig. a, structural phase transition due to the increase of Sr fraction x is noted. For $x=0.0$, all the diffraction peaks are indexed in the rhombohedral structure with $R\bar{3}c$ space group. While, for $x=0.1$ and 0.4 , the structure becomes orthorhombic with $Pbnm$ space group. Refinement values of the structural parameters are gathered in Table 1. The results indicate the increase of the unit cell volume per formula unit with the increase of Sr fraction x , which is coherent with the observed shifts of the diffraction peaks' positions. This increase can be related to the fact that the ionic radius of the strontium ion ($r(\text{Sr}^{2+})=1.31 \text{ \AA}$) is larger than that of the calcium ($r(\text{Ca}^{2+})=1.18 \text{ \AA}$) [45], which leads to an enhancement of the average A-site cationic radius $r_A = \sum x_i r_i$ as well as

Table 1 Results of Rietveld refinement determined from XRD patterns for $\text{La}_{0.6}\text{Ca}_{0.4-x}\text{Sr}_x\text{MnO}_3$ ($x=0.0, 0.1$ and 0.4) compounds

Compound	$x=0.0$	$x=0.1$	$x=0.4$
Space group	$R\bar{3}c$	$Pbnm$	$Pbnm$
a (Å)	5.457 (1)	5.480 (4)	5.507 (1)
b (Å)	5.457 (1)	5.451 (3)	5.461 (1)
c (Å)	13.371 (2)	7.696 (1)	7.733 (1)
V/FU (Å ³)	57.131	57.477	58.140
$\langle \text{Mn} - \text{O} - \text{Mn} \rangle$ (°)	163.9	160.595	159.02
$\langle \text{Mn} - \text{O} \rangle$ (Å)	1.9487	1.959	1.969
r_A (Å)	1.2016	1.2146	1.2536
σ^2 ($10^{-4} \times \text{Å}^2$)	3.11	12.7	21.20
t_G	0.92026	0.92486	0.9386
R_F (%)	1.34	3.05	1.28
R_B (%)	1.7	2.08	1.26
R_p (%)	20.8	14.6	15.4
R_{wp} (%)	14.3	10.5	11.3
R_{exp} (%)	11.18	9.05	8.29
χ^2 (%)	1.733	1.897	1.911

the A-site cation size mismatch $\sigma^2 = \sum x_i r_i^2 - r_A^2$, where x_i and r_i are the atomic fraction and ionic radii of i-type ions at A-site, respectively.

As given in Table 1, the average Mn–O-bond length is found to increase simultaneously with increasing x , whereas the average Mn–O–Mn-bond angle displays the inverse correlation to the variation of the Mn–O-bond length. These results are in good agreement with those found by Radelli et al. [46]. The crystal structure of $\text{La}_{0.6}\text{Ca}_{0.4-x}\text{Sr}_x\text{MnO}_3$ compounds after refinement is introduced in the inset of Fig. 1b–d, respectively. The Mn atom of each sample is coordinated by six oxygen atoms forming an octahedral structure, almost regularly. Based on the evaluated interatomic distances and angles as well as the crystal structure of $\text{La}_{0.6}\text{Ca}_{0.4-x}\text{Sr}_x\text{MnO}_3$, it is clearly apparent that the MnO_6 octahedra are weakly distorted with increasing x .

To confirm the structure of materials, Goldschmidt's tolerance factor t_G as an indicator for the stability and distortion of crystal structure was calculated [47]:

$$t_G = \frac{r_A + r_O}{\sqrt{2}(r_B + r_O)}, \quad (1)$$

where r_A, r_B and r_O are the radii of A, B and O site ions in the ABO_3 structure, respectively.

Oxide-based manganite compounds have a perovskite structure if their tolerance factor is between 0.78 and 1.05 [48]. Departing from Table 1, it is obvious that the values of t_G lie within the stable range of the perovskite structure. The tolerance factor t_G was found to increase with increasing x owing to an increase in the average A-site ionic radius. The increase in t_G leads the system towards more symmetric structure.

It can be observed that in the inset of Fig. 1a, the XRD pattern peaks are broad, indicating the formation of nano-sized $\text{La}_{0.6}\text{Ca}_{0.4-x}\text{Sr}_x\text{MnO}_3$ compounds. The average crystallite size of samples was calculated using the Debye–Scherrer equation [49]:

$$D_{sc} = \frac{K\lambda}{\beta \cos \theta}, \quad (2)$$

where, $\lambda = 1.5406 \text{ \AA}$ is the wavelength of Cu $K\alpha$ radiation, $K = 0.9$ is the shape factor, β is the full-width at half-maximum of an XRD peak in radians and θ is the Bragg angle.

The mean values of the crystallite size, summarized in Table 2, confirm that all compounds are of nanometric size.

The particle-size histogram from the size counting of the nanoparticles garnered from SEM images is presented in Fig. 2. Particles are distributed according to a Lorentzian function [50]. The distribution of particle size can significantly affect the magnetic properties of samples [51]. The mean diameter of samples D_{SEM} is found to lie in the nanometer range (44–60 nm). As can be seen, D_{SEM} is greater than

Table 2 Crystallite size D_{sc} , $\frac{M_{FC}-M_{ZFC}}{M_{FC}} (5K)$, irreversibility temperature T_i , blocking temperature T_B , anisotropy energy KV, Curie temperature T_C , Curie Weiss temperature θ_{CW} , saturation magnetization M_s^{exp} , shell thickness, critical diameter D_c of single domain and the diameter D_{SPM} below which the SPM limit of $\text{La}_{0.6}\text{Ca}_{0.4-x}\text{Sr}_x\text{MnO}_3$ ($x=0.0, 0.1$ and 0.4) compounds occurs

Compound	$x=0.0$	$x=0.4$	$x=0.1$
D_{sc} (nm)	23.8	25.5	30
$\frac{M_{FC}-M_{ZFC}}{M_{FC}} (5K)$	0.524	0.325	0.17
T_i (K)	210	350	295
T_B (K)	150	195	255
$KV (10^{-20}J)$	5.177	6.730	8.802
T_C (K)	255	365	304
θ_{CW} (K)	265	369	310
$M_s^{exp} (\mu_B/Mn)$	2.82	3.00	3.44
t (nm)	0.932	0.753	0.453
D_c (nm)	83.7	51.1	46.3
D_{SPM} (nm)	29.9	30.5	31.8

the size obtained by XRD pattern mainly due to the aggregation of crystallites.

Figure 3 exemplifies the EDAX spectra of all compounds. The analysis was carried out on different zones. One can see that there are no residual side products. All the elements integrated during the preparation (La, Ca, Sr, Mn, and O) are present. The sample composition is similar to the desired one.

3.2 Magnetic measurements

Magnetic measurements as a function of temperature performed according to the standard zero-field cooling (ZFC) and field cooling (FC) procedures, under an applied magnetic field of 0.05 T, are represented in Fig. 4. A net irreversibility between FC and ZFC curves is noted by the appearance of a large bifurcation between the two modes below the irreversible temperature (T_i) (Table 2) [52]. This irreversibility is characterized by $\frac{\Delta M}{M} = \frac{M_{FC}-M_{ZFC}}{M_{FC}}$ at 5 K. It can be associated with the presence of magnetic anisotropy [53–55]. It is known that the response of the spin to the external magnetic field depends on the competition between anisotropy energy and the applied magnetic field strength. At low measuring fields and mainly at low temperature below T_c , all the spins will not be oriented in the direction of the applied magnetic field, indicating the dominance of the magnetic anisotropic field over the applied magnetic field. Hence, the magnitude of M_{ZFC} will depend on the anisotropy. The difference between M_{FC} and M_{ZFC} will be larger for the highly anisotropic compounds. In our study, $\frac{\Delta M}{M}$ is found to increase as particle size decreases (Table 2). Similar

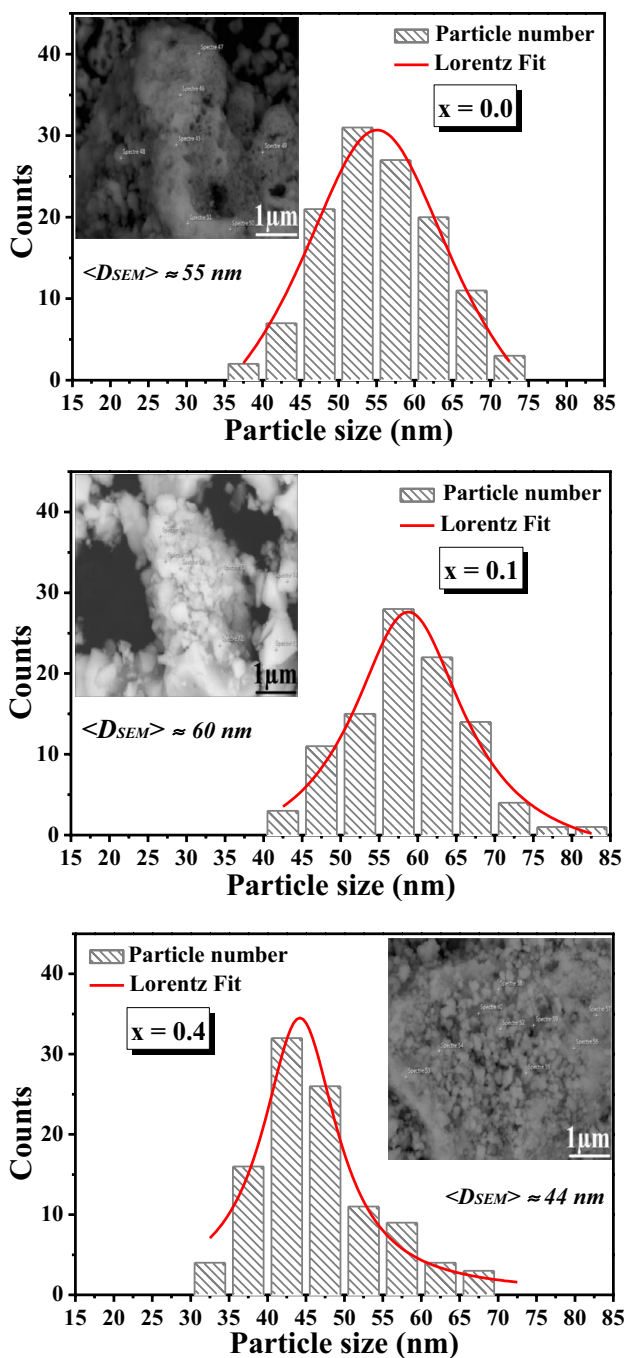


Fig. 2 Size distribution histogram of $\text{La}_{0.6}\text{Ca}_{0.4-x}\text{Sr}_x\text{MnO}_3$ ($x=0.0$, 0.1 and 0.4) compounds. The inset shows the SEM image

results have been reported by Andrade et al. [56]. Such increase of $\frac{\Delta M}{M}$ with the reduction of particle size may be related to the increasing surface/volume ratio, resulting in an increase of magnetic anisotropy. Therefore, it may be concluded that the anisotropy is increased due to surface anisotropy. Results are in good agreement with those reported in the previous studies [57–59], where the authors have argued that surface effects can lead to a variety of

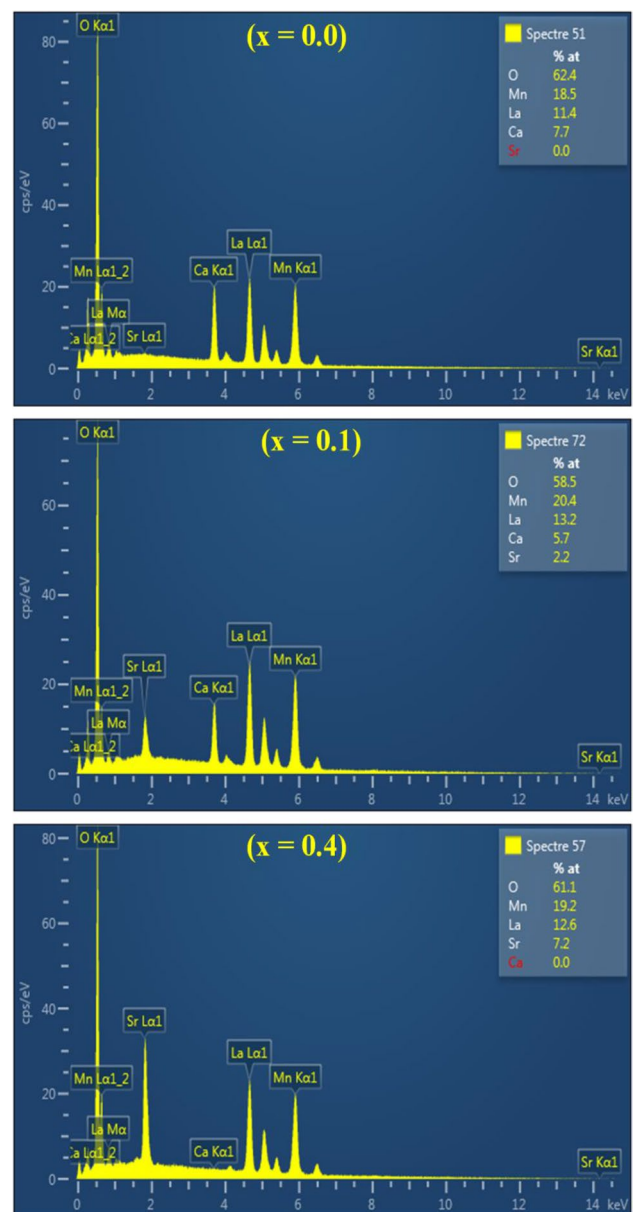


Fig. 3 EDAX analysis spectrum of $\text{La}_{0.6}\text{Ca}_{0.4-x}\text{Sr}_x\text{MnO}_3$ ($x=0.0$, 0.1 and 0.4) compounds

effects in systems of nanoparticles including large anisotropy.

In ZFC procedure, when the system is cooled from room temperature at zero magnetic field, the magnetic moments of the particles are oriented at random. Thus, the total magnetization trends down to zero. Applying an external magnetic field of 0.05 T brings the system to a new magnetic state. The particles start to orient their magnetic moments parallel to the applied field by increasing temperature. The ZFC curve shows a maximum, which corresponds to the blocking temperature (T_B) of system. At this temperature, the thermal energy ($k_B T$) becomes comparable to the anisotropy energy

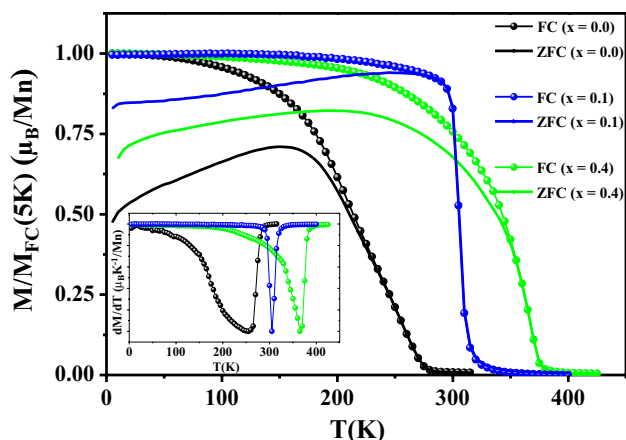


Fig. 4 The temperature dependence of magnetization measured under a magnetic field of 0.05 T, in the ZFC and FC modes for $\text{La}_{0.6}\text{Ca}_{0.4-x}\text{Sr}_x\text{MnO}_3$ ($x=0.0, 0.1$ and 0.4) compounds. The inset presents the plot of dM/dT curve as a function of temperature

(KV) of the system. While, above this temperature, thermal energy dominates the anisotropy energy leading to a quick and spontaneous rotation of magnetic moment of particles and making the system to behave in the SPM regime [60–63]. The observed wide maximum of the ZFC curve is a direct consequence of the noticeable scatter in nanoparticle size as observed previously from the SEM analysis [64, 65]. Each particle gets blocked at a blocking temperature T_B , and the broad nanoparticle distribution range will be associated with the mean value of T_B . Departing from Table 2, it is noticed that T_B increases with the increase in the crystallite size. Similar results have been found in the previous reports [57, 62, 66, 67]. It is well known that the value of T_B strongly depends on the volume of the nanoparticles as follows $KV = 25k_B T_B$ [68], where K is the anisotropy constant containing the volume anisotropy and the surface or interface anisotropy constant [69], V is the volume of nanoparticle and k_B is the Boltzmann constant. The values of the magnetic anisotropy energy KV are displayed in Table 2. For larger particles, the larger volume causes increased anisotropy energy, which decreases the probability of a jump across the anisotropy barrier, and hence, the blocking is shifted to a higher temperature [57].

In the case of the FC measurement, Fig. 4 shows that the magnetization increases in a monotonous way with the temperature decrease. All the samples exhibit a clear magnetic transition from PM to FM state at the Curie temperature T_c , defined as the temperature at which dM/dT shows a minimum (see inset of Fig. 4). The Curie temperatures T_c for all samples are regrouped in Table 2. T_c is found to increase from 255 K for $x=0.0$ to 365 K for $x=0.4$. The increase of T_c should be explained by considering the fact that increasing x increases the average A-site ionic radius r_A which enhances the strength of magnetic exchange interaction

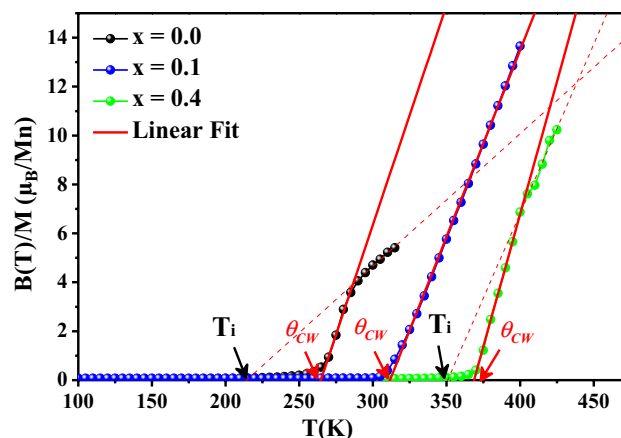


Fig. 5 The temperature dependence of the inverse magnetic susceptibility of FC for $\text{La}_{0.6}\text{Ca}_{0.4-x}\text{Sr}_x\text{MnO}_3$ ($x=0.0, 0.1$ and 0.4) compounds

between Mn^{3+} and Mn^{4+} and favors the FM order that results in shift of Curie temperature to higher temperature [70, 71]. The variation of T_c can also be related to the A-site disorder σ^2 . Obviously, we can see that T_c increases as σ^2 increases. Similar results have been reported in Refs. 71, 72 where the authors show a linear increase of T_c with σ^2 based on the studies of the perovskites with fixed r_A .

The increase in the average crystallite size causes a non-monotonic increase in the Curie temperature. As the proportion of the surface layer in the crystallite volume increases, the ferromagnetism is weakened [73]. This fact explains the minimum values of T_c in the sample with an average crystallite size of ≈ 30 nm. However, an increase in the proportion of the surface layer in the crystallite volume also causes a compression of the unit cell [74] and an enhancement of the exchange interactions. This fact explains an increase in T_c for the sample with an average crystallite size of ≈ 25 nm. The anomalous behavior of the magnetic properties of manganites under investigation can be explained in terms of the competition between the two size effects. Our results are in good agreement with those reported in Trukhanov et al.'s studies [75, 76].

The inverse magnetic susceptibility of FC as a function of temperature $\chi^{-1}(T)$ for all samples is presented in Fig. 5. It is known that the fitting of the inverse magnetic susceptibility $\chi^{-1}(T)$ curve using Curie–Weiss law $1/\chi = (T - \theta_{cw})/C$ [77] provides a valuable information about the magnetic character of material [78–81]. In our case, by fitting the high-temperature region of $\chi^{-1}(T)$, the Curie–Weiss temperature θ_{cw} corresponds to 265, 310 and 369 K for $x=0.0, 0.1$ and 0.4 , respectively (Table 2). The obtained values of θ_{cw} are positive, validating the ferromagnetic character of our samples. Generally, θ_{cw} is slightly higher than T_c which can be associated with the presence of the superparamagnetism phenomenon [50]. However, at higher temperatures, we

note the presence of a clear deviation from the linear region of $\chi^{-1}(T)$ whose extension intersects the temperature axis at T_i . Except for the compound with $x=0.1$, the deviation from the Curie–Weiss law is practically absent which is likely to result from the proximity of the irreversible temperature value ($T_i=295$ K) to the Curie one ($T_c=304$ K). The deviation of $\chi^{-1}(T)$ from the Curie–Weiss law describes the PM/SPM transition at T_i [82, 83]. Presently, we can come to conclude the existence of SPM clusters within the FM phase, in the temperature range between T_B and T_c [50].

Figure 6 shows magnetization hysteresis curves for all samples measured in the temperature range between T_B and T_c , at magnetic fields ranging from -10 to 10 T. These curves clearly indicate that above T_B , nanoparticles under investigation lose their hysteresis property. Zero coercivity and zero remanence are the characteristic features of the SPM behavior of the magnetic nanoparticles [84].

To further analyze the SPM nature of our samples, the magnetization vs. applied magnetic field curves were analyzed using the Langevin function [85, 86] in the framework of the superparamagnetic regime in the Boltzmann equilibrium regime as follows:

$$M(\mu_0 H, T) = M_s \left(\coth \left(\frac{\mu \mu_0 H}{k_B T} \right) - \left(\frac{k_B T}{\mu \mu_0 H} \right) \right), \quad (3)$$

where M_s is the saturation magnetization, k_B is the Boltzmann's constant, and μ is the magnetic moment of the particle.

The best-fit results of our data are demonstrated in Fig. 7, confirming that these samples can be considered as SPM. Comparable findings were reported by Keshri et al. [39]. From this simulation, the saturation magnetizations of compounds were calculated. The values are regrouped in Table 2. It is noted that the saturation magnetization

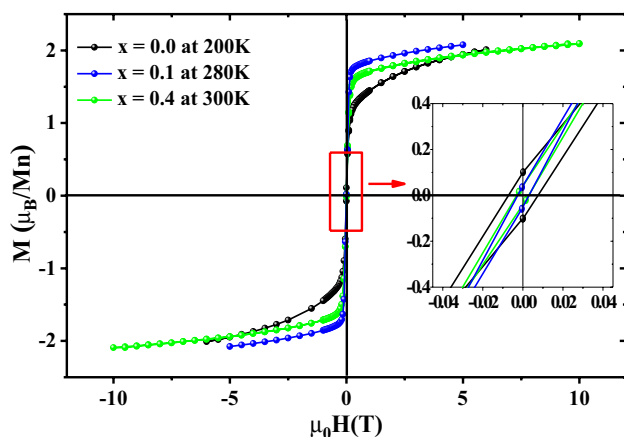


Fig. 6 Hysteresis loop for $x=0.0$ (at 200 K), $x=0.1$ (at 280 K) and $x=0.4$ (at 300 K)

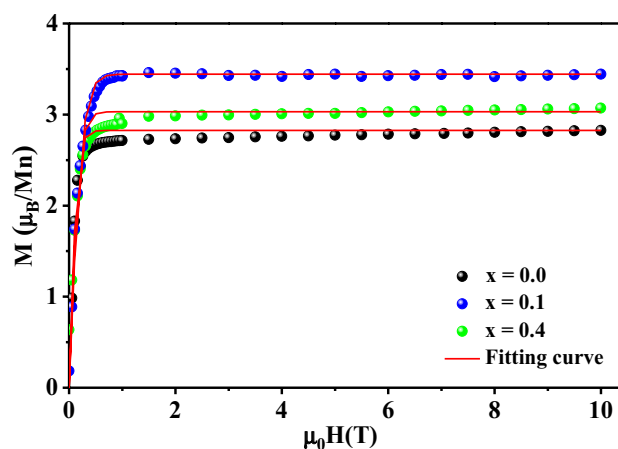


Fig. 7 The applied magnetic field dependence of magnetization $0 \leq \mu_0 H \leq 10$ T measured at a temperature of 5 K for $\text{La}_{0.6}\text{Ca}_{0.4-x}\text{Sr}_x\text{MnO}_3$ ($x=0.0, 0.1$ and 0.4) compounds. The solid line represents the calculation which gives the best fit to experiments

increases with the size of the crystallites. This result can be explained in terms of the Core–shell model [56, 87]. In this model, the core has an FM character, while the shell is ferrimagnetic. The thickness of the shell (t) can be estimated by the following relation [88, 89]:

$$t = \frac{D_{sc}}{2} \left(1 - \sqrt[3]{\frac{M_s^{\text{exp}}}{M_s^{\text{the}}}} \right), \quad (4)$$

where D_{sc} points to the crystallite size, M_s^{exp} is the experimental saturation magnetization obtained from the fitting of M vs. $\mu_0 H$ and M_s^{the} is the theoretical saturation magnetization. As $\text{La}_{0.6}\text{Ca}_{0.4-x}\text{Sr}_x\text{MnO}_3$ ($x=0.0, 0.1$ and 0.4) compounds have a similar ratio of $\text{Mn}^{3+}/\text{Mn}^{4+}$ ($0.6/0.4$), the theoretical saturation magnetization, which is in accordance with the ferromagnetic arrangement, is reported to be $3.6 \mu_B/\text{Mn}$, according to the following expression [50] $M_s^{\text{the}} = g \times \mu_B (0.6 \times S(\text{Mn}^{3+}) + 0.4 \times S(\text{Mn}^{4+}))$, with $S(\text{Mn}^{3+})=2$, $S(\text{Mn}^{4+})=\frac{3}{2}$, 0.6 and 0.4 are the molar fractions of Mn^{3+} and Mn^{4+} , respectively, and $g=2$ is the factor of Landé. The values of t are given in Table 2. We can disclose a clear relationship between the crystallite size, the thickness of the shell, and the saturation magnetization of particles. When the crystallite size becomes smaller, the shell thickness increases which enhances the intercore separation between two neighboring crystallites, resulting in a decrease in the magnetic exchange energy. This explains the reduction of the saturation magnetization [90].

With the reduction of particle size to the nanometric scale, a single domain structure and superparamagnetic regime structure are detected.

The critical diameter D_c below which the system switches from multidomain structure to single magnetic domain structure is given by the relation [91]:

$$D_c = \frac{72\sqrt{AK}}{\mu_0 M_s^2}, \quad (5)$$

where $A = 10^{-11} \text{ J m}^{-1}$ is the exchange constant, K is the uniaxial anisotropy constant, μ_0 is the vacuum permeability, and M_s is the saturation magnetization.

The values of D_c provided in Table 2 are larger than those of the crystallite sizes. Samples under investigation are all considered as single magnetic domain nanoparticles.

The diameter D_{SPM} , below which the nanoparticles can be the seat of SPM phenomenon, is expressed as [50]:

$$D_{\text{SPM}} = \sqrt[3]{\frac{6k_B T}{\pi K} \ln\left(\frac{\tau_m}{\tau_0}\right)}, \quad (6)$$

where k_B is the Boltzmann constant, $T = 300 \text{ K}$ is the temperature, K is the uniaxial anisotropy constant, $\tau_m \approx 100 \text{ s}$ is the average measurement time taken for the thermal energy to flip the magnetization [6] and $\tau_0 \approx 10^{-9} \text{ s}$ is the resonance relaxation time of the spin system [92].

The obtained values of D_{SPM} listed in Table 2 are larger than those of crystallite sizes which strongly confirm the existence of the SPM phenomenon in our compounds.

4 Conclusion

In summary, the structural and magnetic properties of $\text{La}_{0.6}\text{Ca}_{0.4-x}\text{Sr}_x\text{MnO}_3$ for $x = 0.0, 0.1$ and 0.4 nanoparticle compounds have been studied. Rietveld analysis reveals the dependence of structural properties with the increase of Sr content. The nanometric size of samples, estimated using Debye–Scherrer equation and confirmed by SEM images, is at the origin of single domain particle formation and superparamagnetism phenomenon existing below T_c . Magnetization curves as a function of temperature performed according to the standard ZFC and FC processes show a clear PM/FM transition at T_c and the presence of SPM behavior within the FM phase in the temperature range between T_B and T_c where the coercivity and remanence magnetizations are almost zero. The observed irreversibility between FC and ZFC modes was attributed to the presence of magnetic anisotropy which has been explained as arising from the surface effects. The blocking temperature (T_B) was found to be dependent upon the particle size. The evolution of T_c was explained by both the average A-site ionic radius and the A-site cationic disorder. From a theoretical point of view, the SPM behavior has been confirmed by Langevin function for fitting which is found in good agreement with

magnetization vs. magnetic field curves. Saturation magnetization was observed to increase with the increase in particle size giving an evidence for the formation of a magnetically ferrimagnetic layer at the surface.

Compliance with ethical standards

Conflict of interest The authors declare that they have no conflict of interest.

References

1. R. Skomski, *J. Phys. Condens. Mater.* **15**, R841 (2003)
2. G.F. Goya, T.S. Berquo, F.C. Fonseca, M.P. Morales, *J. Appl. Phys.* **94**, 3520 (2003)
3. J. Nogues, V. Skumryev, J. Sort, S. Stoyanov, D. Givord, *Phys. Rev. Lett.* **97**, 157203 (2006)
4. B.D. Cullity, *Introduction to Magnetic Materials* (Addison-Wesley, Reading, 1972)
5. A. Rostamnejadi, H. Salamati, P. Kameli, H. Ahmadvand, *J. Magn. Magn. Mater.* **321**, 3126 (2009)
6. L. Neel, *C.R. Acad. Sci. Paris* **228**, 664 (1949)
7. J.L. Dormann, L. Bessais, D. Fiorani, *J. Phys. C Solid State Phys.* **21**, 2015 (1988)
8. J.L. Dormann, D. Fiorani, R. Cherkaoui, E. Tronc, F. Lucari, F. D'Orazio, L. Spinu, M. Nogues, H. Kachkchi, J.P. Jolivet, *J. Magn. Magn. Mater.* **203**, 23 (1999)
9. A. Verma, T.C. Goel, R.G. Mendiratta, *Mater. Sci. Technol.* **16**, 712 (2000)
10. J.D.G. Durán, J.L. Arias, V. Gallardo, A.V. Delgado, *J. Pharm. Sci.* **97**, 2948 (2008)
11. V.P. Torchilin, *Eur. J. Pharm. Sci.* **11**, 81 (2000)
12. I. Sharifi, H. Shokrollahi, S. Amiri, *J. Magn. Magn. Mater.* **324**, 903 (2012)
13. A. Ito, Y. Kuga, H. Honda, H. Kikkawa, A. Horiuchi, Y. Watanabe, T. Kobayashi, *Cancer Lett.* **212**, 167 (2004)
14. R. Ivkov, S.J. DeNardo, W. Daum, A.R. Foreman, R.C. Goldstein, V.S. Nemkov, G.L. DeNardo, *Clin. Cancer Res.* **11**, 7093s (2005)
15. K.M. Krishnan, *IEEE Trans. Magn.* **46**, 2523 (2010)
16. W. Schütt, C. Grüttner, J. Teller, F. Westphal, U. Häfeli, B. Paulke, W. Finck, *J. Artif. Organs.* **23**, 98 (1999)
17. A.V. Trukhanov, M.A. Almessiere, A. Baykal, S.V. Trukhanov, Y. Slimani, D.A. Vinnik, V.E. Zhivulin, A.Yu. Starikov, D.S. Klygach, M.G. Vakhitov, T.I. Zubar, D.I. Tishkevich, E.L. Trukhanova, M. Zdorovets, *J. Alloys Compd.* **788**, 1193 (2019)
18. A.V. Trukhanov, M.A. Darwish, L.V. Panina, A.T. Morchenko, V.G. Kostishyn, V.A. Turchenko, D.A. Vinnik, E.L. Trukhanova, K.A. Astapovich, A.L. Kozlovskiy, M. Zdorovets, S.V. Trukhanov, *J. Alloys Compd.* **791**, 522 (2019)
19. S.V. Trukhanov, A.V. Trukhanov, V.A. Turchenko, V.G. Kostishyn, L.V. Panina, I.S. Kazakevich, A.M. Balagurov, *J. Alloys Compd.* **689**, 383 (2016)
20. A.V. Trukhanov, V.G. Kostishyn, L.V. Panina, S.H. Jabarov, V.V. Korovushkin, S.V. Trukhanov, E.L. Trukhanova, *Ceram. Int.* **43**, 12822 (2017)
21. M.A. Almessiere, Y. Slimani, H. Güngüne, A. Bayka, S.V. Trukhanov, A.V. Trukhanov, *Nanomaterials* **9**, 24 (2019)
22. A. Tozri, E. Dhahri, E.K. Hlil, *Mater. Lett.* **64**, 2138 (2010)
23. M. Khlifi, A. Tozri, M. Bejar, E. Dhahri, E.K. Hlil, *J. Magn. Magn. Mater.* **324**, 2142 (2012)

24. R. Tlili, M. Bejar, E. Dhahri, A. Zaoui, E.K. Hlil, L. Bessais, *Polyhedron* **121**, 19 (2017)
25. A. Dhahri, M. Jemmal, E. Dhahri, M.A. Valente, *J. Alloy. Compd.* **638**, 221 (2015)
26. I.O. Troyanchuk, S.V. Trukhanov, H. Szymczak, J. Przewoznik, K. Bärner, *JETP* **93**, 161 (2001)
27. S.V. Trukhanov, N.V. Kasper, I.O. Troyanchuk, M. Tovar, H. Szymczak, K. Bärner, *J. Solid State Chem.* **169**, 85 (2002)
28. I.O. Troyanchuk, S.V. Trukhanov, H. Szymczak, K. Baerner, *J. Phys. Condens. Matter* **12**, L155 (2000)
29. S.V. Trukhanov, I.O. Troyanchuk, I.M. Fita, H. Szymczak, K. Bärner, *J. Magn. Magn. Mater.* **237**, 276–282 (2001)
30. S.V. Trukhanov, *J. Mater. Chem.* **13**, 347 (2003)
31. A.A. Kuznetsov, O.A. Shlyakhtin, N.A. Brusentsov, O.A. Kuznetsov, *Eur. Cells Mater.* **3**, 75 (2002)
32. V. Uskokovic, A. Kosak, M. Drogenik, *Int. J. Appl. Ceram. Technol.* **3**, 134 (2006)
33. N.D. Thorat, S.V. Otari, R.A. Bohara, H.M. Yadav, V.M. Khot, A.B. Salunkhe, M.R. Phdatre, A.I. Prasad, R.S. Ningthoujam, S.H. Pawar, *Mater. Sci. Eng. C* **42**, 637 (2014)
34. S.V. Trukhanov, L.S. Lobanovski, M.V. Bushinsky, V.A. Khomchenko, N.V. Pushkarev, I.O. Tyoyanchuk, A. Maignan, D. Flahaut, H. Szymczak, R. Szymczak, *Eur. Phys. J. B* **42**, 51 (2004)
35. S.V. Trukhanov, *JETP* **100**, 95 (2005)
36. S.V. Trukhanov, I.O. Troyanchuk, A.V. Trukhanov, I.M. Fita, A.N. Vasil'ev, A. Maignan, H. Szymczak, *JETP Lett.* **83**, 33 (2006)
37. H. Asano, S.B. Ogale, J. Garrison, A. Orozoco, Y.H. Li, V. Smolyaninova, C. Gally, M. Downes, M. Rajeshwari, R. Ramesh, T. Venkatesan, *Appl. Phys. Lett.* **74**, 3696 (1999)
38. R. Rajagopal, J. Mona, S.N. Kale, T. Bala, R. Pasricha, P. Poddar, M. Sastry, B.L.V. Prasad, D.C. Kundaliya, S.B. Ogale, *Appl. Phys. Lett.* **89**, 023107 (2006)
39. S. Keshri, S. Biswas, P. Wisniewski, *J. Alloy. Compd.* **656**, 245 (2016)
40. M. Horiki, T. Nakagawa, S. Seino, T.A. Yamamoto, *J. Magn. Magn. Mater.* **329**, 49 (2013)
41. V.A. Atsarkin, A.A. Generalov, V.V. Demidov, A.E. Mefed, M.N. Markelova, OYu. Gorbenko, A.R. Kaul, E.J. Roy, B.M. Odintsov, *J. Magn. Magn. Mater.* **321**, 3198 (2009)
42. O.V. Melnikov, OYu. Gorbenko, M.N. Popova, A.R. Kaul, V.A. Atsarkin, V.V. Demidov, E.J. Roy, C. Soto, B.M. Odintsov, *J. Biomed. Mater. Res. A* **91**, 1048 (2009)
43. M.A. Almessiere, A.V. Trukhanov, Y. Slimani, K.Y. You, S.V. Trukhanov, E.L. Trukhanova, F. Esa, A. Sadaqat, K. Chaudhary, M. Zdorovets, A. Baykal, *Nanomaterials* **9**, 202 (2019)
44. J. Rodrigues-Carvajal, *FULLPROF: A Rietveld Refinement and Pattern Matching Analysis Program* (CEA-CNRS, France, 2000)
45. R.D. Shannon, *Acta Crystallogr. Sect. A* **32**, 751 (1976)
46. P.G. Radaelli, G. Iannone, M. Marezio, H.Y. Hwang, S.-W. Cheong, J.D. Jorgensen, D.N. Argyriou, *Phys. Rev. B* **56**, 8265 (1997)
47. V.M. Goldschmidt, *Geochemistry* (Oxford University Press, Oxford, 1958)
48. C.A. Randall, A.S. Bhalla, T.R. Shrout, L.E.J. Cross, *Mater. Res.* **5**, 829 (1990)
49. P. Sherrer, *Göttinger Nachrichten* **2**, 98 (1918)
50. H. Gharsallah, A. Souissi, M. Bejar, E. Dhahri, E.K. Hlil, *Mater. Chem. Phys.* **182**, 429 (2016)
51. A.C. Gandhi, P.M. Reddy, T.S. Chan, Y.P. Ho, S.Y. Wu, *RSC Adv.* **5**, 84782 (2015)
52. G. Madhu, K. Maniammal, V. Biju, *Phys. Chem. Chem. Phys.* **18**, 12135 (2016)
53. S. Umashankar, T. Parida, K.R. Kumar, A.M. Strydom, G. Markandeyulu, K.K. Bharathi, *J. Magn. Magn. Mater.* **439**, 213 (2017)
54. Y. Kalyana Lakshmi, G. Venkataiah, P.V. Reddy, *J. Appl. Phys.* **106**, 023707 (2009)
55. L. Liu, Y. Liu, J. Miao, Z. Lü, X. Wang, Y. Sui, W. Su, *J. Alloy. Compd.* **427**, 11 (2007)
56. V.M. Andrade, R.J. Caraballo-Vivas, T. Costas-Soares, S.S. Pedro, D.L. Rocco, M.S. Reis, A.P.C. Campos, A.A. Coelho, *J. Solid. Stat. Chem.* **219**, 87 (2014)
57. K. Maaz, A. Mumtaz, S.K. Hasanain, A.J. Ceylan, *J. Magn. Magn. Mater.* **308**, 289 (2007)
58. M. Knobel, W.C. Nunes, L.M. Socolovsky, E. De Biasi, J.M. Vargas, J. C. Denardin **8**, 2836 (2008)
59. R.H. Kodama, *J. Magn. Magn. Mater.* **200**, 359 (1999)
60. W. Cai, J. Wan, *J. Colloid, Interface Sci.* **305**, 366 (2007)
61. T. Zhang, G. Li, T. Qian, J.F. Qu, X.Q. Xiang, X.G. Li, *J. Appl. Phys.* **100**, 094324 (2006)
62. S. Roy, I. Dubenko, D.D. Ederh, N. Ali, *J. Appl. Phys.* **96**, 1202 (2004)
63. R.W. Li, H. Xiong, J.R. Sun, Q.A. Li, Z.H. Wang, J. Zhang, B.G. Shen, *J. Phys. Condens. Matter* **13**, 141 (2001)
64. P. Fernández-García, P. Gorria, M. Sevilla, M.P. Proença, R. Boada, J. Chaboy, J.A. Blanco, *J. Phys. Chem. C* **115**, 5294 (2011)
65. V.M. Kalita, D.M. Polishchuk, D.G. Kovalchuk, A.V. Bodnaruk, S.O. Solopan, A.I. Tovstolytkin, A.G. Belous, *Phys. Chem. Chem. Phys.* **19**, 27015 (2017)
66. M.P. Proença, C.T. Sousa, A.M. Perceira, P.B. Tavares, J. Ventura, M. Vaquez, J.P. Araujo, *Phys. Chem. Chem. Phys.* **13**, 9561 (2011)
67. N. Rinaldi-Montes, P. Gorria, D. Martinez-Blanco, A.B. Fuertes, L. Fernandez Barquin, *Nanoscale* **6**, 457 (2014)
68. M. Khan, J. Duan, Y. Chen, H. Yao, S. Lyu, H. Shou, Q. Xu, *J. Alloy. Compd.* **701**, 147 (2017)
69. P. Bruno, J.P. Renard, *Appl. Phys. A* **49**, 499 (1989)
70. A. Tozri, M. Bejar, E. Dhahri, E.L. Hlil, *Open Phys.* **7**, 89 (2009)
71. A. Berenov, F. Le Goupil, N. Alford, *Sci. Rep.* **6**, 28055 (2016)
72. D. Sinclair, J. áPaul Attfield, *Chem. Commun.* **16**, 1497 (1999)
73. P. Dey, T.K. Nath, *Phys. Rev. B Condens. Matter* **73**, 214–425 (2006)
74. N. Das, P. Mondal, D. Bhattacharya, *Phys. Rev. B Condens. Matter* **74**, 014–410 (2006)
75. S.V. Trukhanov, A.V. Trukhanov, C.E. Botez, A.H. Adair, H. Szymczak, R. Szymczak, *J. Phys. Condens. Matter* **19**, 266214 (2007)
76. S.V. Trukhanov, A.V. Trukhanov, S.G. Stepin, H. Szymczak, C.E. Botez, *Phys. Solid State* **50**, 886 (2008)
77. A.H. Morrish, *The Physical Principles of Magnetism* (Wiley-VCH, Hoboken, 2001)
78. P.S. Behera, P.A. Bhoje, *J. Magn. Magn. Mater.* **394**, 200 (2015)
79. H.M. Rai, S.K. Saxena, V. Mishra, A. Sagdeo, P. Rajput, R. Kumar, P.R. Sagdeo, *J. Mater. Chem. C* **4**, 10876 (2016)
80. A. Sagdeo, K. Gautam, P.R. Sagdeo, M.N. Singh, S.M. Gupta, A.K. Nigam, R. Rawat, A.K. Sinha, H. Ghosh, T. Ganguli, A. Chakrabarti, *Appl. Phys. Lett.* **105**, 042906 (2014)
81. F. Issaoui, M.T. Tlili, M. Bejar, E. Dhahri, E.K. Hlil, *J. Supercond. Nov. Magn.* **25**, 1169 (2012)
82. C. Djega-Mariadassou, L. Bessaïs, J.L. Dormann, G. Villers, *J. Phys.* **49**, C8–1825 (1988)
83. F.J. Lazaro, A. Lopez, A. Larrea, Q.A. Pankhurst, J.M. Lopez Nieto, A. Corma, *IEEE Trans. Magn.* **34**, 1030 (1998)
84. G. Aravind, M. Raghasudha, D. Ravinder, *J. Magn. Magn. Mater.* **378**, 278 (2015)
85. P. Langevin, *Magnétisme et théorie des electrons. Ann. Chim. Phys.* **5**, 70 (1905)
86. T. Ozkaya, M.S. Toprak, A. Baykal, H. Kavas, Y. Köseoğlu, B. Aktaş, *J. Alloy. Compd.* **472**, 18 (2009)
87. M. Secu, M. Cernea, C.E. Secu, B.S. Vasile, *Mater. Chem. Phys.* **151**, 81 (2015)
88. S.B. Xi, W.J. Lu, H.Y. Wu, P. Tong, Y.P. Sun, *J. Appl. Phys.* **112**, 123903 (2012)

89. H.M. El-Sayed, I.A. Ali, A. Azzam, A.A. Sattar, J. Magn. Mater. **424**, 226 (2017)
90. M.H. Ehsani, P. Kameli, M.E. Ghazi, F.S. Razavi, M. Taheri, J. Appl. Phys. **114**, 223907 (2013)
91. A.P. Guimaraes, *Principles of Nanomagnetism, NanoScience and Technology* (Springer, Berlin, 2009)
92. W.F. Brown, Phys. Rev. **130**, 1677 (1963)

Publisher's Note Springer Nature remains neutral with regard to jurisdictional claims in published maps and institutional affiliations.